

Finding the Order in Complexity: The Electronic Structure of 14-1-11 Zintl Compounds

Yukun Liu*,¹ Michael Y. Toriyama*,¹ Zizhen Cai,¹ Mengjia Zhao,¹ Fei Liu,¹ and G. Jeffrey Snyder^{‡1}

Department of Materials Science and Engineering, Northwestern University, Evanston, IL, USA, 60208

(Dated: 10 October 2021)

$\text{Yb}_{14}\text{MnSb}_{11}$ and $\text{Yb}_{14}\text{MgSb}_{11}$ have rapidly risen to prominence as high-performing p-type thermoelectric materials for potential deep space power generation. However, the fairly complex crystal structure of 14-1-11 Zintl compounds renders the interpretation of the electronic band structure obscure, making it difficult to chemically guide band engineering and optimization efforts. In this work, we delineate the valence-balanced Zintl chemistry of $A_{14}MX_{11}$ compounds ($A = \text{Yb}, \text{Ca}$; $M = \text{Mg}, \text{Mn}, \text{Al}, \text{Zn}, \text{Cd}$; $X = \text{Sb}, \text{Bi}$) using molecular orbital theory analysis. By analyzing the electronic band structures of $\text{Yb}_{14}\text{MgSb}_{11}$ and $\text{Yb}_{14}\text{AlSb}_{11}$, we show that the conduction band minimum is composed of either an antibonding molecular orbital originating from the $(\text{Sb}_3)^{7-}$ trimer, or a mix of atomic orbitals of A , M , and X . The singly degenerate valence band is comprised of non-bonding Sb p_z orbitals primarily from the Sb atoms in the $(\text{MSb}_4)^{m-}$ tetrahedra and the of isolated Sb atoms distributed throughout the unit cell. Such a chemical understanding of the electronic structure enables strategies to engineer electronic properties (e.g., the band gap) of $A_{14}MX_{11}$ compounds.

¹ * Y.L. and M.Y.T. contributed equally to this work.

[‡] jeff.snyder@northwestern.edu

Thermoelectric materials can reversibly and directly convert heat into electricity with no moving parts. However, the energy conversion efficiencies of current thermoelectric devices remain insufficient for widespread applications. Thermoelectric energy conversion efficiency is thermodynamically limited by the Carnot efficiency and depends on the material figure of merit ($zT = \alpha^2 \sigma T / \kappa$)¹. Conceptually, to obtain a large zT , a large Seebeck coefficient (α) and electrical conductivity (σ) are desired, while the thermal conductivity (κ) should be minimized. However, because these properties are highly interrelated and all good thermoelectric materials behave as heavily doped semiconductors², engineering zT is best understood as optimizing the charge carrier concentration n and maximizing the thermoelectric quality factor $B \sim \mu_W / \kappa_L$ where μ_W is the weighted mobility³ and κ_L is the lattice thermal conductivity.

The weighted mobility depends on the electronic structure through the effective mass and valley degeneracy but also the electron scattering. Generally, a complex band structure with high effective valley degeneracy is desired⁴ while flat bands with high band effective mass are detrimental to mobility^{5,6}. In addition, the character of the bands can help determine how strong a substitutional atom will scatter electrons or holes by how much it alters the conduction or valence band.

The optimal charge carrier concentration is engineered by intrinsic defects and extrinsic substitutional atoms where an understanding of the Zintl chemistry is essential⁷.

The discovery⁸ of the complex Zintl compound, $\text{Yb}_{14}\text{MnSb}_{11}$ as a high zT , high-temperature (900 K – 1300 K), p-type thermoelectric material has paved the way for 20% or more efficient thermoelectric power generation such that it has been selected by NASA for next-generation radioisotope thermoelectric generators (RTGs) for space missions⁹. With improved processing, and various chemical substitutions of the A or M atom in $A_{14}MSb_{11}$ several examples with $zT > 1$ have been reported¹⁰. All of the compounds have exceptionally low lattice thermal conductivity (κ_L) because of the large unit cell¹¹ that limits propagating acoustic waves to a small frequency range and so most of the heat is transported by diffusons¹².

Despite the complex structure, a number of chemical variations are known with the $A_{14}MX_{11}$ structure (Figure 1), many with similar electronic properties.¹³ The A atom is generally a +2 cation such as Yb^{14,15}, Ca^{15,16}, and Eu^{17,18} where +3 Rare Earth elements (e.g. La¹⁹ and Y²⁰) can be substituted. The M atom can be a variety of transition metals

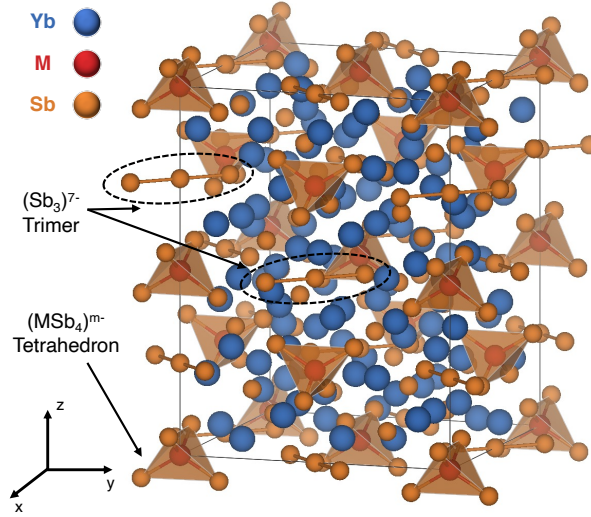


FIG. 1. The unit cell of $\text{Yb}_{14}\text{MSb}_{11}$ ($M = \text{Mg}, \text{Mn}, \text{Al}, \text{Zn}, \text{or Cd}$). Yb atoms are indicated by blue spheres, Sb atoms are brown, Sb_3 linear units are shown as bonded brown atoms, and $(\text{MSb}_4)^{m-}$ are indicated by brown tetrahedra where m is 9 for $M = \text{Mn}, \text{Al}$ and 10 for $M = \text{Mg}, \text{Zn}, \text{Cd}$.

suitable for centering the MX_4 tetrahedron (such as $M = \text{Mg}^{15}, \text{Mn}^8, \text{Al}^{21}, \text{Zn}^{22}, \text{or Cd}^{23}$). The X atom can be any of the pnictides ($\text{Sb}^{15}, \text{As}^{24}$ or Bi^{16}).

From detailed experimental and theoretical analysis of the high zT compositions $\text{Yb}_{14}\text{MnSb}_{11}$ and $\text{Yb}_{14}\text{MgSb}_{11}$ and related compounds it has been shown^{15,23,25-28} that the valence bands are essentially the same for the Sb compounds. The valence bands contain a simple, light valence band with a second heavier valence band close in energy that has high valley degeneracy which provides additional conduction paths, contributing to a high electrical conductivity, while maintaining a large thermopower^{5,6}.

The electronic structure and chemical tunability of $\text{Yb}_{14}\text{MSb}_{11}$ can be generally explained using Zintl Chemistry⁷. Zintl compounds can be described as a network of covalently bonded complex anions with charge balanced by cations donating their valence electrons²⁹. Thus, the valence of an atom can be defined as follows:

$$V_c = e_c - b_c \quad (1)$$

$$V_a = e_a + b_a - 8 \quad (2)$$

where V represents the valence, e is the number of valence electrons, and b is the number

of formed bonds, while c and a denote cations and anions, respectively. Each bond between anions or between cations reduces the magnitude of the valence by 1. Utilizing this charge counting method, the complex structure of $\text{Yb}_{14}\text{MSb}_{11}$ can be described as consisting of $(\text{MSb}_4)^{m-}$ ($m = 9$ or 10) isolated tetrahedra, $(\text{Sb}_3)^{7-}$ linear units, and isolated Yb^{2+} and Sb^{3-} ions. The value of m depends on the valence of the atom on the M site. When M is trivalent, like Al^{3+} , $m = 9$ and the compound is a valence balanced semiconductor. When M is divalent, like Mg^{2+} , $m = 10$ and the compounds are slightly electron poor making a p-type metal or heavily doped semiconductor. This system of charge counting has enabled tuning of the free charge carrier concentration in $A_{14}\text{MSb}_{11}$ compounds by substituting some A and M atoms with others of a different valence^{30,31}

Another way to understand the chemistry of the Zintl compounds is to combine the Zintl concept with molecular orbital analysis³². This method has been successfully applied to half-Heusler compounds to interpret band structures based on the characteristics of molecular orbitals³³. The high symmetry of the clearly distinguished $(\text{MSb}_4)^{m-}$ and $(\text{Sb}_3)^{7-}$ structural units renders possibilities of identifying their molecular orbitals in the electronic structure to interpret the complex band structures.

In this study, we will focus on interpreting the computed band structures of two $\text{Yb}_{14}\text{MSb}_{11}$ compounds: $\text{Yb}_{14}\text{MgSb}_{11}$ and $\text{Yb}_{14}\text{AlSb}_{11}$ using the Zintl concept in combination with a molecular orbital analysis. We show that the molecular orbitals for structural units $(\text{MSb}_4)^{m-}$, and $(\text{Sb}_3)^{7-}$ are easily identified giving clear indication as to which atoms dominate the conduction and valence bands. We discuss how this method can be used to understand and modify the electronic properties of $A_{14}\text{MX}_{11}$ compounds providing strategies to optimize their thermoelectric performance. All first-principles Density Functional Theory (DFT) calculations were performed using the Vienna *ab-initio* simulation package (VASP)^{34–39} using the projector-augmented wave (PAW) method^{40,41} and an energy cutoff of 500 eV. The 4f electrons of Yb were not treated explicitly as valence electrons following the methodology of Ref. 25. The structures were relaxed with a force convergence criterion of 0.005 eV/Å with a Γ -centered k -point grid⁴² of $3 \times 3 \times 3$. Static calculations were subsequently performed on the relaxed structures with a k -point grid of $5 \times 5 \times 5$ using the tetrahedron method⁴³ for density of states calculations.

The electronic structures of $\text{Yb}_{14}\text{MgSb}_{11}$ and $\text{Yb}_{14}\text{AlSb}_{11}$ exhibit many overlapping bands (Figure 2), owing to the large number of atoms in the unit cells. Despite the complexity, the

band structures reveal distinctive features based on the structural chemistry of the $(\text{Sb}_3)^{7-}$ trimers and $(\text{MSb}_4)^{m-}$ tetrahedra.

The Fermi energy is at the valence band maximum when M in $A_{14}MX_{11}$ is trivalent (e.g., Al^{3+} , see Figure 2b), since there are 14 nonbonding Yb^{2+} atoms, 4 nonbonding Sb^{3-} atoms, a single $(\text{MSb}_4)^{9-}$ tetrahedral unit, and a single $(\text{Sb}_3)^{7-}$ trimer per formula unit. The valence-balanced $\text{Yb}_{14}\text{AlSb}_{11}$ therefore exhibits semiconductor behavior.³⁰ In contrast, the Fermi energy is buried in a partially-filled valence band when M is divalent (e.g., Mg^{2+} , see Figure 2a). $\text{Yb}_{14}\text{MgSb}_{11}$ is therefore deficient of one electron per formula unit, according to charge counting: $14\text{Yb}^{2+} + (\text{MgSb}_4)^{10-} + (\text{Sb}_3)^{7-} + 4\text{Sb}^{3-} + 1\text{h}^+$. This indicates that the valence band is partially filled and explains why the compound exhibits behaviors of a heavily doped semiconductor.²⁹

The conduction bands are largely dominated by Yb-s states, and one can therefore expect the energies of the conduction bands to be affected by the electronegativity of the A cation in $A_{14}MX_{11}$. The unoccupied conduction bands are also mixed with Sb-p and Al-p character from the $(\text{Sb}_3)^{7-}$ trimers and $(\text{MSb}_4)^{m-}$ tetrahedra. Notably, there are four distinctly low-energy conduction bands that are isolated from the rest of the conduction bands in $\text{Yb}_{14}\text{MgSb}_{11}$, which we call the σ^* bands (Figure 3a). These bands form a narrow peak in the DOS ~ 1 eV above the Fermi energy (Figure 2a) and are primarily of $(\text{Sb}_3)^{7-}$ character. The charge density distribution of the σ^* bands (Figure 3a) shows that the bands are antibonding states of the $(\text{Sb}_3)^{7-}$ trimer unit. The antibonding character is evidenced by the nodal features of the charge density, where the wave function is zero between the middle Sb atom and the ends of the trimer, owing to the destructive interference of p-orbitals aligned along the axis of the trimer unit.

The σ^* bands are critical in that they resolve differences in the conduction band structures of 14-1-11 compounds. For example, we can identify the same σ^* bands in $\text{Yb}_{14}\text{AlSb}_{11}$ (Figure 3b), only they are not isolated from the rest of the conduction bands in this compound. This difference can be attributed to the M cation in $A_{14}MX_{11}$. In $\text{Yb}_{14}\text{MSb}_{11}$ compounds, the conduction bands are separated into those that are purely of $(\text{Sb}_3)^{7-}$ character (i.e., the σ^* bands) and those that are higher in energy. The latter group of conduction bands have partial M character, meaning that the bands will be lower in energy in $\text{Yb}_{14}\text{AlSb}_{11}$ than in $\text{Yb}_{14}\text{MgSb}_{11}$ due to the higher electronegativity of Al. We also do not expect the absolute energies of the σ^* bands to differ significantly between the two compounds, as the $(\text{Sb}_3)^{7-}$

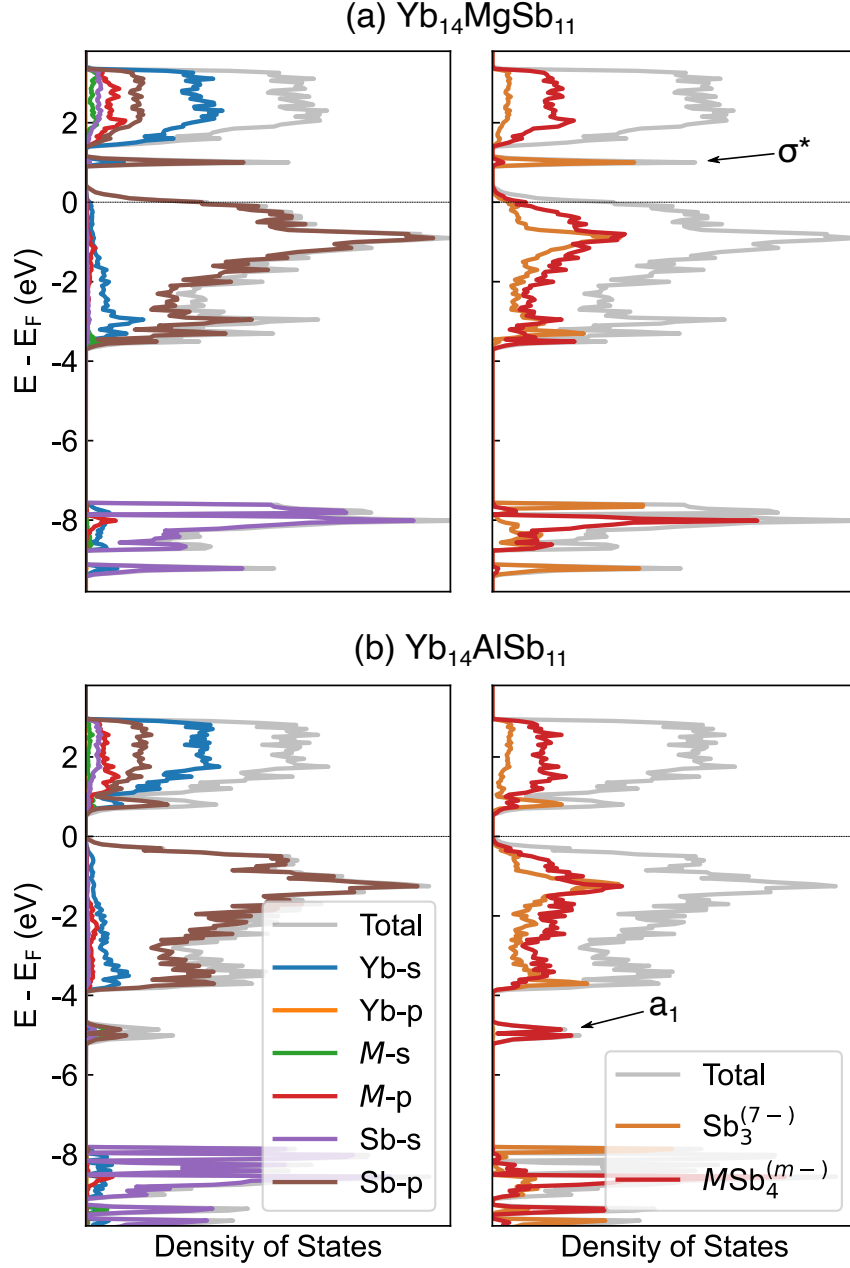


FIG. 2. Density of states of (a) $\text{Yb}_{14}\text{MgSb}_{11}$ and (b) $\text{Yb}_{14}\text{AlSb}_{11}$. The partial density of states of the $(\text{Sb}_3)^{7-}$ trimers, and the MSb_4 tetrahedra are also shown. The σ^* states are labeled in the $\text{Yb}_{14}\text{MgSb}_{11}$ panel, and the a_1 states are labeled in the $\text{Yb}_{14}\text{AlSb}_{11}$ panel.

trimer units exist in both compounds. It is as if the higher-energy conduction bands of $\text{Yb}_{14}\text{AlSb}_{11}$ have “descended” in energy, merging with the σ^* bands unlike in $\text{Yb}_{14}\text{MgSb}_{11}$.

The valence bands on the other hand are primarily of Sb character, with the p-orbitals contributing to the bands from ~ 4 eV below the Fermi energy up to the valence band

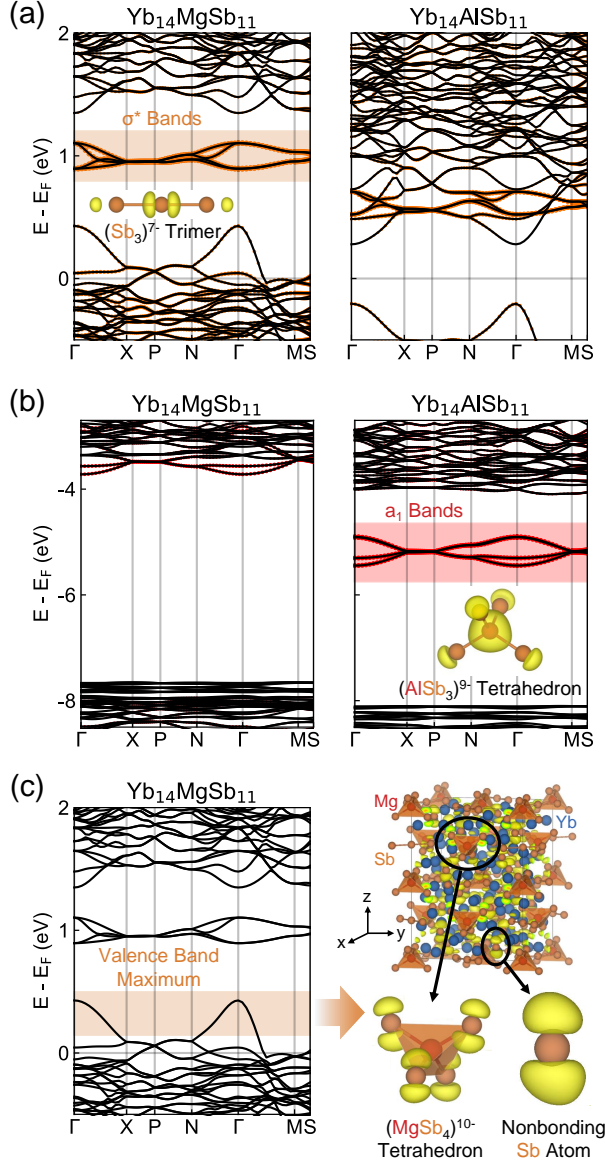


FIG. 3. (a) Band structures of Yb₁₄MgSb₁₁ and Yb₁₄AlSb₁₁, where the size of the orange circles correspond to the relative contributions from the (Sb₃)⁷⁻ trimers to the bands. The charge density of Yb₁₄MgSb₁₁ within the orange highlighted portion of the band structure is localized only on the (Sb₃)⁷⁻ trimers, as shown for one trimer unit. (b) Band structures plotted within a lower energy range, where contributions from the Mg/Al atoms are shown as red circles. The charge density of Yb₁₄AlSb₁₁ within the pink highlighted portion is localized only on the (AlSb₄)⁹⁻ tetrahedra, as shown for one unit. (c) The band structure of Yb₁₄MgSb₁₁, highlighting the energy window of the valence band for which the charge density is calculated. The charge density near the valence band maximum is dominated by the nonbonding Sb p_z orbitals primarily on the (MgSb₄)¹⁰⁻ tetrahedra and nonbonding Sb atoms, with some contribution from the trimer.

maximum (VBM) and the s-orbitals contributing to the bands located ~ 8 eV below the Fermi energy (Figure 2). Similar to the σ^* conduction bands, we can distinguish features of the valence bands between $\text{Yb}_{14}\text{AlSb}_{11}$ and $\text{Yb}_{14}\text{MgSb}_{11}$. Notably, an isolated set of peaks appears in the DOS ~ 5 eV below the Fermi energy in $\text{Yb}_{14}\text{AlSb}_{11}$ that is not present in $\text{Yb}_{14}\text{MgSb}_{11}$. There are four bands that contribute to the peaks (the a_1 bands), which are mainly comprised of Al-s and Sb-p atomic orbitals in $\text{Yb}_{14}\text{AlSb}_{11}$, as evidenced by both the partial density of states (Figure 2b) and the orbital-decomposed band structure (Figure 3b). Moreover, the charge density distribution of the a_1 bands (Figure 3b) suggests that the states are of bonding character. While the a_1 bands are isolated from the rest of the valence bands in $\text{Yb}_{14}\text{AlSb}_{11}$, orbital contributions from Mg indicates that the a_1 bands are merged into the other valence bands in $\text{Yb}_{14}\text{MgSb}_{11}$ (Figure 3b). The difference in the electronic structures can again be attributed to the higher electronegativity of Al, which lowers the energies of the a_1 bands in $\text{Yb}_{14}\text{AlSb}_{11}$ relative to those in $\text{Yb}_{14}\text{MgSb}_{11}$.

The valence band maximum is a singly-degenerate, relatively light band which emerges from the flatter valence bands at the Γ point (Figure 3c). The charge density of this band exhibits p_z -type orbitals centered on the Sb atoms of the $(\text{MSb}_4)^{m-}$ tetrahedra and non-bonding Sb atoms (Figure 3c) with less contribution from the trimer. The fact that only the p_z orbitals of Sb atoms make up the light valence band suggests that hole transport should be somewhat anisotropic with different electrical conductivity in the x and y directions. We note that the valence bands in $A_{14}\text{MSb}_{11}$ compounds are quite similar, with a single dispersive band centered at the Γ point and flatter, non-dispersive bands below the band extremum (see e.g., $\text{Yb}_{14}\text{MnSb}_{11}$ ²⁵). The fact that these bands are dominated by Sb-atoms explains why the p-type thermoelectric properties of all $A_{14}\text{MSb}_{11}$ compounds are similar for the same hole concentration.

Despite the complex electronic structure of $\text{Yb}_{14}\text{MSb}_{11}$, many distinguishing features can be explained using molecular orbital theory⁴⁴ and Zintl chemistry.³² The structural makeup of $\text{Yb}_{14}\text{MSb}_{11}$ compounds consists of $(\text{Sb}_3)^{7-}$ trimers, $(\text{MSb}_4)^{m-}$ tetrahedra, isolated Sb anions, and isolated Yb cations. These components generate bands at different energy ranges due to the energies of the atomic orbitals and bonding/antibonding interactions.

The $(\text{Sb}_3)^{7-}$ linear trimer unit is isoelectronic to the triiodide ion I_3^- and therefore has similar molecular orbitals (Figure 4a).^{24,32,45} The relative phases of the Sb-p orbitals in $(\text{Sb}_3)^{7-}$ lead to distinct molecular orbital energies based on whether the neighboring interactions are

bonding, antibonding, or nonbonding, as well as their configurations (i.e., whether they are σ - or π -oriented, see Figure 4a). When the p-orbitals of all three Sb atoms align in-phase along the axis of the trimer unit, the lowest-energy σ bonding state will form. However, if the neighboring interactions are out-of-phase instead, then the highest-energy σ^* antibonding state will form. Due to the linear structure of the $(\text{Sb}_3)^{7-}$ trimer, there is only one σ bonding state and one σ^* antibonding state. Additionally, the p-orbitals of the Sb atoms can align perpendicular to the axis of the trimer unit, forming doublet π bonding and doublet π^* antibonding states. The π and π^* states are closer in energy than the σ and σ^* states, as π -bonds are typically weaker than σ -bonds³². Moreover, there are nonbonding states both in the σ and π configurations. In total, each $(\text{Sb}_3)^{7-}$ trimer unit contributes nine bands (two σ -type, four π -type, and three nonbonding) to the electronic structure of $\text{Yb}_{14}\text{MSb}_{11}$, of which eight are filled with two electrons each. The one unfilled state, the σ^* molecular orbital, should appear in the conduction bands of $\text{Yb}_{14}\text{MSb}_{11}$. As a matter of fact, the σ^* molecular orbital in Figure 4a corresponds precisely to the σ^* bands in Figure 3a: the four σ^* bands come from the four $(\text{Sb}_3)^{7-}$ trimer units per primitive cell of $\text{Yb}_{14}\text{MSb}_{11}$, and the charge density distribution of the σ^* bands indicate antibonding character.

The molecular orbital diagram of the $(\text{AlSb}_4)^{9-}$ tetrahedral unit (Figure 4b) is constructed following the methodology of Toriyama et al.⁴⁶ The bonding a_1 state of $(\text{AlSb}_4)^{9-}$ is a molecular orbital in which the a_1 state of the Sb_4 complex, which appears as dumbbell-like orbitals at each corner of the tetrahedron oriented towards the central Al atom, interferes constructively with the s-orbital of the central Al atom. Due to the constructive interference, we expect the charge density for the a_1 state to be high between the central Al atom and the surrounding Sb_4 complex, as in the charge density shown in Figure 3b. On the other hand, the destructive interference leads the formation of a_1^* state. Moreover, we expect from molecular orbital theory that the a_1 bonding state of $(\text{AlSb}_4)^{9-}$ consists of Al-s, Sb-s, and Sb-p character by symmetry, all of which are reflected in the a_1 peaks in the orbital-decomposed DOS in Figure 2b. As a result, the a_1 bands in $\text{Yb}_{14}\text{MSb}_{11}$ correspond exactly to the a_1 bonding state shown in Figure 4b as expected from molecular orbital theory, where we have four a_1 bands since there are four $(\text{MSb}_4)^{m-}$ tetrahedral units per primitive cell.

A chemical intuition for the electronic structures of $\text{Yb}_{14}\text{MgSb}_{11}$ and $\text{Yb}_{14}\text{AlSb}_{11}$ described here can guide band engineering efforts of $A_{14}MX_{11}$ compounds in general, as similar electronic structures have been observed in this class of materials. For example, charge

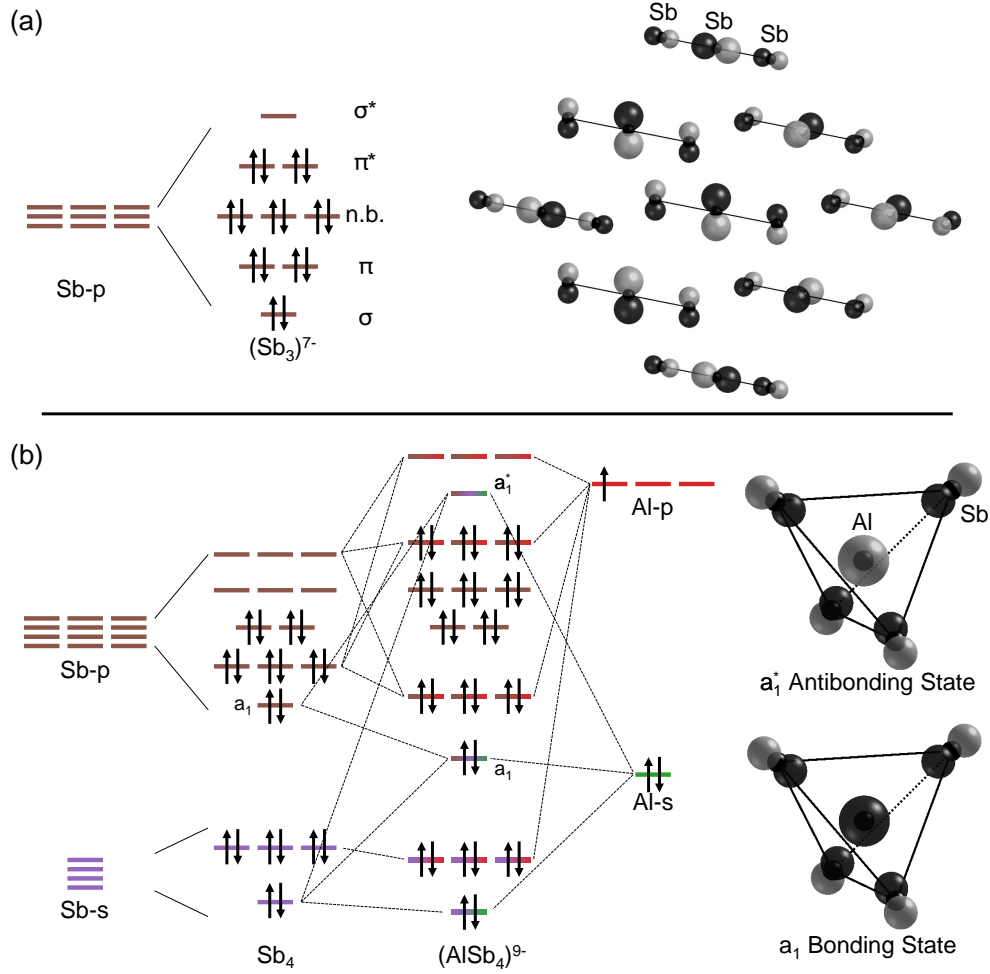


FIG. 4. (a) The molecular orbital diagram for a $(\text{Sb}_3)^{7-}$ trimer unit in $A_{14}\text{MSb}_{11}$, where the molecular orbitals are constructed from the p-orbitals of the Sb atoms. The p-orbitals of the Sb atoms generate nine molecular orbitals in total, two of which are σ -type singlet states, four π states, and a triplet set of nonbonding (n.b.) states. (b) The molecular orbital diagram for the $(\text{AlSb}_4)^{9-}$ tetrahedral unit of $\text{Yb}_{14}\text{AlSb}_{11}$. The a_1 state generated by the Sb-p orbitals hybridizes with the s-orbital of Al, forming a bonding a_1 state and an antibonding a_1^* state. The shading of the molecular orbitals denotes the relative phases.

density contour plots²⁴ of the $(\text{As}_3)^{7-}$ trimer unit in $\text{Ca}_{14}\text{GaAs}_{11}$ are reminiscent of the molecular orbitals derived for the $(\text{Sb}_3)^{7-}$ trimer in Figure 4a. The antibonding σ^* bands from the trimer unit is also observed in many compounds with the same structure type, regardless of whether the σ^* bands are isolated from the other conduction bands ($\text{Ca}_{14}\text{MgSb}_{11}$,¹³ $\text{Yb}_{14}\text{MnSb}_{11}$,²⁵ $\text{Ca}_{14}\text{MnBi}_{11}$,⁴⁵ $\text{Ca}_{14}\text{MgBi}_{11}$,⁴⁷ $\text{Sr}_{14}\text{ZnAs}_{11}$ ⁴⁸) or merged into the higher-energy

conduction bands ($\text{Ca}_{14}\text{AlBi}_{11}$,¹⁶ $\text{Ba}_{14}\text{MnBi}_{11}$,⁴⁵ $\text{Ca}_{14}\text{ZnSb}_{11}$,⁴⁹ $\text{Sr}_{14}\text{CdSb}_{11}$ ²³).

The conduction band minimum is determined by the relative energies of the σ^* bands originating from the $(X_3)^{7-}$ trimers and the nonbonding A orbitals, and the valence band maximum at the Γ point is determined by the energies of the p_z orbitals of X atoms that are either nonbonding or involved in the $(MX_4)^{m-}$ tetrahedral units. This may explain the saturation in the measured Seebeck coefficient of $\text{Yb}_{14-x}\text{Pr}_x\text{MnSb}_{11}$ with increasing Pr content,⁵⁰ where the band gap remains unchanged past a certain Pr content likely due to the fixed energies of the Sb-derived band edges.

In summary, despite their complex structures, the electronic structures of $A_{14}MX_{11}$ compounds can be understood using Zintl chemistry in combination with molecular orbital theory. The derived bonding/antibonding interactions within the structural units successfully explain the electronic structures calculated using first-principles, building a chemical intuition for $A_{14}MX_{11}$ compounds.

ACKNOWLEDGMENTS

We thank Trinh Vo, Susan Kauzlarich and Paul von Allmen for preliminary work and helpful discussions. This work was supported by NSF DMREF award #1729487. M.Y.T. is funded by the United States Department of Energy through the Computational Science Graduate Fellowship (DOE CSGF) under grant number DE-SC0020347. This research was supported in part through the computational resources and staff contributions provided for the Quest high performance computing facility at Northwestern University, which is jointly supported by the Office of the Provost, the Office for Research, and Northwestern University Information Technology.

DATA AVAILABILITY

The data that support the findings of this study are available from the corresponding author upon reasonable request.

AUTHOR DECLARATIONS

Conflict of interest

The authors have no conflicts to disclose.

REFERENCES

- ¹G. J. Snyder and E. S. Toberer, “Complex thermoelectric materials,” *Nat. Mater.* **7**, 105 (2008).
- ²X. Zhang, Z. Bu, X. Shi, Z. Chen, S. Lin, B. Shan, M. Wood, A. H. Snyder, L. Chen, G. J. Snyder, and Y. Pei, “Electronic quality factor for thermoelectrics,” *Science Advances* **6**, eabc0726 (2020).
- ³G. J. Snyder, A. H. Snyder, M. Wood, R. Gurunathan, B. H. Snyder, and C. Niu, “Weighted mobility,” *Adv. Mater.* **32**, 2001537 (2020).
- ⁴Z. M. Gibbs, F. Ricci, G. Li, H. Zhu, K. Persson, G. Ceder, G. Hautier, A. Jain, and G. J. Snyder, “Effective mass and fermi surface complexity factor from ab initio band structure calculations,” *npj Comput. Mater.* **3**, 1 (2017).
- ⁵Y. Pei, H. Wang, and G. J. Snyder, “Band engineering of thermoelectric materials,” *Adv. Mater.* **24**, 6125 (2012).
- ⁶Y. Pei, A. D. LaLonde, H. Wang, and G. J. Snyder, “Low effective mass leading to high thermoelectric performance,” *Energ. Environ. Sci.* **5**, 7963 (2012).
- ⁷E. S. Toberer, A. F. May, and G. J. Snyder, “Zintl chemistry for designing high efficiency thermoelectric materials,” *Chem. Mater.* **22**, 624 (2010).
- ⁸S. R. Brown, S. M. Kauzlarich, F. Gascoin, and G. J. Snyder, “Yb₁₄mnsb₁₁: New high efficiency thermoelectric material for power generation,” *Chem. Mater.* **18**, 1873 (2006).
- ⁹S. Kauzlarich and S. K. Bux, “Earth abundant high temperature materials for radioisotope power conversion system,” *Tech. Rep.* (University of California, 2016).
- ¹⁰A. P. Justl, G. Cerretti, S. K. Bux, and S. M. Kauzlarich, “Hydride assisted synthesis of the high temperature thermoelectric phase: Yb₁₄mgsb₁₁,” *J. Appl. Phys.* **126**, 165106 (2019).
- ¹¹E. S. Toberer, A. Zevalkink, and G. J. Snyder, “Phonon engineering through crystal chemistry,” *J. Mater. Chem.* **21**, 15843–15852 (2011).

- ¹²R. Hanus, J. George, M. Wood, A. Bonkowski, Y. Cheng, D. L. Abernathy, M. E. Manley, G. Hautier, G. J. Snyder, and R. P. Hermann, “Uncovering design principles for amorphous-like heat conduction using two-channel lattice dynamics,” *Mater. Today Phys.* **18**, 100344 (2021).
- ¹³Y. Hu, G. Cerretti, E. L. K. Wille, S. K. Bux, and S. M. Kauzlarich, “The remarkable crystal chemistry of the $\text{Ca}_{14}\text{AlSb}_{11}$ structure type, magnetic and thermoelectric properties,” *J. Solid State Chem.* **271**, 88 (2019).
- ¹⁴Y. Hu and S. M. Kauzlarich, “ $\text{Yb}_{14}\text{MgBi}_{11}$: structure, thermoelectric properties and the effect of the structure on low lattice thermal conductivity,” *Dalton T.* **46**, 3996 (2017).
- ¹⁵Y. Hu, J. Wang, A. Kawamura, K. Kovnir, and S. M. Kauzlarich, “ $\text{Yb}_{14}\text{MgSb}_{11}$ and $\text{Ca}_{14}\text{MgSb}_{11}$ – new Mg-containing zintl compounds and their structures, bonding, and thermoelectric properties,” *Chem. Mater.* **27**, 343 (2015).
- ¹⁶S. Baranets and S. Bobev, “ $\text{Ca}_{14}\text{AlBi}_{11}$ – a new zintl phase from earth-abundant elements with a great potential for thermoelectric energy conversion,” *Mater. Today Adv.* **7**, 100094 (2020).
- ¹⁷J. Y. Chan, S. M. Kauzlarich, P. Klavins, R. N. Shelton, and D. J. Webb, “Colossal magnetoresistance in the transition-metal zintl compound $\text{Eu}_{14}\text{MnSb}_{11}$,” *Chem. Mater.* **9**, 3132 (1997).
- ¹⁸W.-j. Tan, Y.-t. Liu, M. Zhu, T.-j. Zhu, X.-b. Zhao, X.-t. Tao, and S.-q. Xia, “Structure, magnetism, and thermoelectric properties of magnesium-containing antimonide zintl phases $\text{Sr}_{14}\text{MgSb}_{11}$ and $\text{Eu}_{14}\text{MgSb}_{11}$,” *Inorg. Chem.* **56**, 1646 (2017).
- ¹⁹E. S. Toberer, S. R. Brown, T. Ikeda, S. M. Kauzlarich, and G. Jeffrey Snyder, “High thermoelectric efficiency in lanthanum doped $\text{Yb}_{14}\text{MnSb}_{11}$,” *Appl. Phys. Lett.* **93**, 062110 (2008).
- ²⁰E. L. Kunz Wille, N. S. Grewal, S. K. Bux, and S. M. Kauzlarich, “Seebeck and figure of merit enhancement by rare earth doping in $\text{Yb}_{14-x}\text{RE}_x\text{ZnSb}_{11}$ ($x=0.5$),” *Materials* **12**, 731 (2019).
- ²¹E. S. Toberer, C. A. Cox, S. R. Brown, T. Ikeda, A. F. May, S. M. Kauzlarich, and G. J. Snyder, “Traversing the metal-insulator transition in a zintl phase: rational enhancement of thermoelectric efficiency in $\text{Yb}_{14}\text{Mn}_{1-x}\text{Al}_x\text{Sb}_{11}$,” *Adv. Funct. Mater.* **18**, 2795 (2008).
- ²²I. Fisher, S. Bud’Ko, C. Song, P. Canfield, T. Ozawa, and S. M. Kauzlarich, “ $\text{Yb}_{14}\text{ZnSb}_{11}$: charge balance in zintl compounds as a route to intermediate Yb valence,” *Phys. Rev. Lett.*

- 85**, 1120 (2000).
- ²³J. P. Makongo, G. M. Darone, S.-Q. Xia, and S. Bobev, “Non-stoichiometric compositions arising from synergistic electronic and size effects. synthesis, crystal chemistry and electronic properties of $A_{14}cd_{1+x}Pn_{11}$ compounds ($0 \leq x \leq 0.3$; $A = sr, eu$; $Pn = as, sb$),” *J. Mater. Chem. C* **3**, 10388 (2015).
- ²⁴R. Gallup, C. Fong, and S. M. Kauzlarich, “Bonding properties of calcium gallium arsenide, $ca_{14}gaas_{11}$: a compound containing discrete $gaas_4$ tetrahedra and a hypervalent as_3 polyatomic unit,” *Inorg. Chem.* **31**, 115 (1992).
- ²⁵C. J. Perez, M. Wood, F. Ricci, G. Yu, T. Vo, S. K. Bux, G. Hautier, G.-M. Rignanese, G. J. Snyder, and S. M. Kauzlarich, “Discovery of multivalley fermi surface responsible for the high thermoelectric performance in $yb_{14}mnsb_{11}$ and $yb_{14}mgsb_{11}$,” *Science Advances* **7**, eabe9439 (2021).
- ²⁶Y. Wang, Y.-J. Hu, S. A. Firdosy, K. E. Star, J.-P. Fleurial, V. A. Ravi, L.-Q. Chen, S.-L. Shang, and Z.-K. Liu, “First-principles calculations of lattice dynamics and thermodynamic properties for $yb_{14}mnsb_{11}$,” *J. Appl. Phys.* **123**, 045102 (2018).
- ²⁷J. Xu and H. Kleinke, “Unusual sb–sb bonding in high temperature thermoelectric materials,” *J. Comput. Chem.* **29**, 2134 (2008).
- ²⁸Y. Hu, K. Lee, and S. M. Kauzlarich, “Optimization of $ca_{14}mgsb_{11}$ through chemical substitutions on sb sites: Optimizing seebeck coefficient and resistivity simultaneously,” *Crystals* **8**, 211 (2018).
- ²⁹S. M. Kauzlarich, *Chemistry, Structure, and Bonding of Zintl Phases and Ions*, 1st ed. (Wiley VCH, 1996).
- ³⁰E. S. Toberer, C. A. Cox, S. R. Brown, T. Ikeda, A. F. May, S. M. Kauzlarich, and G. J. Snyder, “Traversing the metal-insulator transition in a zintl phase: Rational enhancement of thermoelectric efficiency in $yb_{14}mn_{1-x}al_xsb_{11}$,” *Adv. Funct. Mater.* **18**, 2795 (2008).
- ³¹E. S. Toberer, S. R. Brown, T. Ikeda, S. M. Kauzlarich, and G. Jeffrey Snyder, “High thermoelectric efficiency in lanthanum doped $yb_{14}mnsb_{11}$,” *Appl. Phys. Lett.* **93**, 062110 (2008), <https://doi.org/10.1063/1.2970089>.
- ³²J. Xu and H. Kleinke, “Unusual sb-sb bonding in high temperature thermoelectric materials,” *J. Comput. Chem.* **29**, 2134 (2008).
- ³³W. G. Zeier, J. Schmitt, G. Hautier, U. Aydemir, Z. M. Gibbs, C. Felser, and G. J. Snyder, “Engineering half-Heusler thermoelectric materials using zintl chemistry,” *Nat.*

- Rev. Mater. **1**, 1 (2016).
- ³⁴G. Kresse, “Ab initio molecular dynamics for liquid metals,” *J. Non-Cryst. Solids* **192**, 222 (1995).
- ³⁵G. Kresse and J. Furthmüller, “Efficiency of ab-initio total energy calculations for metals and semiconductors using a plane-wave basis set,” *Comp. Mater. Sci.* **6**, 15 (1996).
- ³⁶G. Kresse and J. Furthmüller, “Efficient iterative schemes for ab initio total-energy calculations using a plane-wave basis set,” *Phys. Rev. B* **54**, 11169 (1996).
- ³⁷S. Maintz, B. Eck, and R. Dronskowski, “Speeding up plane-wave electronic-structure calculations using graphics-processing units,” *Comput. Phys. Commun.* **182**, 1421 (2011).
- ³⁸M. Hacene, A. Anciaux-Sedrakian, X. Rozanska, D. Klahr, T. Guignon, and P. Fleurat-Lessard, “Accelerating vasp electronic structure calculations using graphic processing units,” *J. Comput. Chem.* **33**, 2581 (2012).
- ³⁹M. Hutchinson and M. Widom, “Vasp on a gpu: Application to exact-exchange calculations of the stability of elemental boron,” *Comput. Phys. Commun.* **183**, 1422 (2012).
- ⁴⁰P. E. Blöchl, “Projector augmented-wave method,” *Phys. Rev. B* **50**, 17953 (1994).
- ⁴¹G. Kresse and D. Joubert, “From ultrasoft pseudopotentials to the projector augmented-wave method,” *Phys. Rev. B* **59**, 1758 (1999).
- ⁴²H. J. Monkhorst and J. D. Pack, “Special points for brillouin-zone integrations,” *Phys. Rev. B* **13**, 5188 (1976).
- ⁴³P. E. Blöchl, O. Jepsen, and O. K. Andersen, “Improved tetrahedron method for brillouin-zone integrations,” *Phys. Rev. B* **49**, 16223 (1994).
- ⁴⁴T. A. Albright, J. K. Burdett, and M.-H. Whangbo, *Orbital interactions in chemistry* (John Wiley & Sons, 2013).
- ⁴⁵D. Sánchez-Portal, R. M. Martin, S. M. Kauzlarich, and W. Pickett, “Bonding, moment formation, and magnetic interactions in $\text{ca}_{14}\text{mnbi}_{11}$ and $\text{ba}_{14}\text{mnbi}_{11}$,” *Phys. Rev. B* **65**, 144414 (2002).
- ⁴⁶M. Toriyama, M. Brod, and G. J. Snyder, “Chemical interpretation of charged point defects in semiconductors: A case study of mg_2si ,” *ChemRxiv* (2021), 10.33774/chemrxiv-2021-729bm.
- ⁴⁷W. Tan, Z. Wu, M. Zhu, J. Shen, T. Zhu, X. Zhao, B. Huang, X.-t. Tao, and S.-q. Xia, “ $\text{A}_{14}\text{mgbi}_{11}$ ($A = \text{ca}, \text{sr}, \text{eu}$): Magnesium bismuth based zintl phases as potential thermoelectric materials,” *Inorg. Chem.* **56**, 10576 (2017).

- ⁴⁸S. Baranets, G. M. Darone, and S. Bobev, “Synthesis and structure of $\text{sr}_{14}\text{zn}_{1+x}\text{as}_{11}$ and $\text{eu}_{14}\text{zn}_{1+x}\text{as}_{11}$ ($x \leq 0.5$). new members of the family of pnictides isotypic with $\text{ca}_{14}\text{alsb}_{11}$, exhibiting a new type of structural disorder,” *J. Solid State Chem.* **280**, 120990 (2019).
- ⁴⁹S. Baranets and S. Bobev, “From the ternary phase $\text{ca}_{14}\text{zn}_{1+\delta}\text{sb}_{11}$ ($\delta 0.4$) to the quaternary solid solutions $\text{ca}_{14-x}\text{RE}_x\text{znsb}_{11}$ ($\text{RE} = \text{la, nd, sm, gd, x 0.9}$). a tale of electron doping via rare-earth metal substitutions and the concomitant structural transformations,” *Inorg. Chem.* **58**, 8506 (2019).
- ⁵⁰Y. Hu, S. K. Bux, J. H. Grebenkemper, and S. M. Kauzlarich, “The effect of light rare earth element substitution in $\text{yb}_{14}\text{mnsb}_{11}$ on thermoelectric properties,” *J. Mater. Chem. C* **3**, 10566 (2015).